Ensemble prediction for nowcasting with a convection-permitting model - II: forecast error statistics

Article

Published Version

Tellus
SERIES A
DYNAMIC
METEOROLOGY
AND OCEANOGRAPHY
PUBLISHED BY THE INTERNATIONAL METEOROLOGICAL INSTITUTE IN STOCKHOLM

Tellus (2011), 63A, 497–512
Printed in Singapore. All rights reserved

TELLUS

Ensemble prediction for nowcasting with a convection-permitting model – II: forecast error statistics

By R. N. BANNISTER[1]*, S. MIGLIORINI[1] and M. A. G. DIXON[2], [1]*National Centre for Earth Observation, Department of Meteorology, University of Reading, Earley Gate, Reading, RG6 6BB, UK;* [2]*Met Office Joint Centre for Mesoscale Meteorology, Department of Meteorology, University of Reading, Earley Gate, Reading, RG6 6BB, UK*

(Manuscript received 14 April 2010; in final form 29 November 2010)

ABSTRACT

A 24-member ensemble of 1-h high-resolution forecasts over the Southern United Kingdom is used to study short-range forecast error statistics. The initial conditions are found from perturbations from an ensemble transform Kalman filter. Forecasts from this system are assumed to lie within the bounds of forecast error of an operational forecast system. Although noisy, this system is capable of producing physically reasonable statistics which are analysed and compared to statistics implied from a variational assimilation system. The variances for temperature errors for instance show structures that reflect convective activity. Some variables, notably potential temperature and specific humidity perturbations, have autocorrelation functions that deviate from 3-D isotropy at the convective-scale (horizontal scales less than 10 km). Other variables, notably the velocity potential for horizontal divergence perturbations, maintain 3-D isotropy at all scales. Geostrophic and hydrostatic balances are studied by examining correlations between terms in the divergence and vertical momentum equations respectively. Both balances are found to decay as the horizontal scale decreases. It is estimated that geostrophic balance becomes less important at scales smaller than 75 km, and hydrostatic balance becomes less important at scales smaller than 35 km, although more work is required to validate these findings. The implications of these results for high-resolution data assimilation are discussed.

1. Introduction

The latest breed of models which are now becoming available for routine weather forecasting have a grid length of a kilometre or so (Lean et al., 2008). Such models are expected to yield skill in predicting fine scale weather events, such as convective storms, at lead times of up to a few hours when used with appropriate data assimilation techniques (Dixon et al., 2009). The forecasting problems to overcome at such resolutions (termed 'convective-scale' or 'storm-scale') are different to those which have been dealt with in lower resolution systems (e.g. at 'synoptic-scales'). In some respects the convective-scale modelling problem becomes simpler as the grid length decreases, due to the diminishing need to parametrize convection (e.g. Lean et al., 2008). The problem of accurately and appropriately determining the initial conditions of such models is, however, arguably becoming more difficult owing to the lack of useful knowledge about the characteristics of forecast uncertainty at convective scales.

Knowledge of forecast uncertainty is represented by a forecast error covariance matrix, $\mathbf{P}^{\mathrm{f}}$, and is a vital ingredient for data assimilation as it describes how an a priori state, $\mathbf{x}^{\mathrm{b}}$ (an estimate of the initial conditions before observations are considered, which comes from a previous forecast) is allowed to be updated by observations (e.g. Bannister, 2008a). $\mathbf{P}^{\mathrm{f}}$ cannot be stored explicitly in large data assimilation problems but there are a number of ways in which $\mathbf{P}^{\mathrm{f}}$ can be approximated for data assimilation. One way is to use the information present in an ensemble of forecasts to imply the $\mathbf{P}^{\mathrm{f}}$ matrix, as done in the ensemble Kalman filter (e.g. Lorenc, 2003b). This method is found to rely too heavily on the ensemble alone, which in practice will have very many fewer members than the number of data points to determine. This leads to problems of undersampling such as filter divergence and spurious covariances (e.g. Ehrendorfer, 2007). Another way is to build a model of $\mathbf{P}^{\mathrm{f}}$ that reproduces features that $\mathbf{P}^{\mathrm{f}}$ is thought to have. This is the approach used in 3-D and 4-D variational data assimilation systems (e.g. Lorenc, 2003a) where the matrix used

*Corresponding author.
e-mail: r.n.bannister@reading.ac.uk
DOI: 10.1111/j.1600-0870.2010.00500.x

to model $\mathbf{P}^{\mathrm{f}}$ is conventionally called the **B**-matrix. In variational data assimilation (VAR) systems that operate at synoptic- and global-scales, it is usual that the model of the **B**-matrix implies forecast error covariances that obey near geostrophic and exact hydrostatic balances, are homogeneous and isotropic in space, and are stationary in time (e.g. Bannister, 2008b). Although not ideal, these simplifications give rise to data assimilation systems that do a reasonable job at producing analysis increments at the scales they were designed for.

This paper is concerned with forecast error covariances derived from a high-resolution limited area model (LAM), which is a version of the Met Office Unified Model centred on a domain over Southern United Kingdom with a grid length of 1.5 km. Due to the high resolution it is expected that the forecast error covariances have elements that violate the larger scale properties mentioned above. For instance, it is known that geostrophic and hydrostatic balances diminish in convective-scale flows (although it is not known precisely at what scale this process starts to become important), and that the forecast error covariances are likely to become more flow dependent (e.g. Zhang, 2005). For a variational data assimilation method to be applicable in convective-scale problems, new ways of formulating **B** which are appropriate to the finer scales are being sought.

Before this process can begin various questions arise, as little is known about the properties of forecast uncertainty at convective-scales. Here, this problem is studied by examining a selection of forecast error statistics derived from a 24-member ensemble of high-resolution forecasts generated from a version of the 'Met Office Global and Regional Ensemble Prediction System' (MOGREPS, Bowler et al., 2008) adapted for use with the 1.5 km model (Migliorini et al., 2011). Studying an ensemble at a fixed time, rather than over an extended period (the latter as in Fisher, 2003; Buehner, 2005; Berre et al., 2006) or with the NMC method (Parrish and Derber, 1992) allows us to examine a snapshot of forecast error statistics. It is possible to look at only a small selection of covariance diagnostics, but it is hoped that those shown in this paper will help later to focus the development of a suitable model of **B** that is applicable to the convective-scale VAR problem. The following issues are raised in this paper:

(i) Can useful information be extracted from an ensemble with a relatively small number of members?

(ii) How does forecast uncertainty change with the flow?

(iii) What is the typical spatial structure of forecast error covariances?

(iv) To what degree does hydrostatic and geostrophic balance hold at these scales?

These are difficult issues to address. Apart from dealing with forecast data from a non-linear model with a large state space, the tool that is being used to help answer these questions (i.e. statistics from a relatively small ensemble) itself introduces noise (e.g. Houtekamer and Mitchell, 2001). For these reasons, this work comprises a mix of qualitative and quantitative results to help address these points.

This paper has the following structure: In Section 2 the model's domain is shown, the MOGREPS system is introduced and the meteorological case chosen for study is introduced. In Sections 3–6 a selection of ensemble-derived statistics is shown for the high-resolution model (and sometimes a coarser model for comparison): variances (Section 3), point structure functions (Section 4), correlations in vertical cross-sections (Section 5) and balance-related diagnostics (Section 6). In Section 7 the work is reviewed and concluded.

2. The SUK-1.5 model, the source of the ensemble perturbations and the case study considered

The model used primarily in this study covers a 540 $\times$ 432 km domain over Southern United Kingdom (Lean et al., 2008), which is here designated SUK-1.5. It has a horizontal grid length of 1.5 km and 70 vertical eta levels with a top at 40 km and a vertical spacing ranging from a few tens of metres in the boundary layer to a few kilometres near the top. It is nested inside the 7340 $\times$ 4400 km domain of the North Atlantic and European model (here designated NAE), itself having a horizontal grid length of 24 km for ensemble forecasts, which provides the lateral boundary conditions for SUK-1.5. The domain of the NAE model is shown in fig. 1 of Bowler et al. (2008). The NAE itself is nested inside a global model, which has 90 km horizontal grid length at mid-latitudes. The Met Office also runs other LAMs operationally of intermediate grid length (e.g. 4 km), which are not considered in this study. All of these models have the same formulation of the dynamical core (Davies et al., 2005), but SUK-1.5 does not rely on parametrized convection as it is supposed to be of high enough resolution to permit convective effects without one, although it is probably not of high enough resolution to resolve convective processes fully.

The ensemble prediction system MOGREPS, Bowler et al. (2008), is an application of the ensemble transform Kalman filter, Bishop et al. (2001), which generates a set of perturbations, which are then added to a control analysis. This procedure results in an ensemble of states centred around the analysis which is designed to have the correct analysis error covariance among its members for the given observation network. The ensemble of short (1-h) forecasts from each member (including the control) is then expected to hold useful information about forecast error covariances, which are studied in this work.

The forecast error covariance statistics derived from the forecast ensemble are accurate, strictly speaking, only in the limit of an ensemble with an infinite number of members. A small (23-member plus control) ensemble will lead to sampling error, which we do not attempt to quantify in this paper. Although we expect many diagnostics of the statistics to be useful, sampling error is a limitation of this work, but is unavoidable for a

number of reasons. First, increasing the number of members cannot be done at present without a complete redesign of the system and then running the increased number of members through a hierarchy of progressively smaller scale models. Second, doing temporal averaging of statistics will improve their accuracy, but doing this will remove important flow-dependent information of interest. Third, doing localization of error covariances would eliminate some of the sampling error, but doing this is thought to lead to spurious balance diagnostics (Kepert, 2009), which may actually invalidate parts of the work here, especially in Section 6. We attempt to justify the use of a small ensemble at appropriate places in this paper.

The MOGREPS system has been recently adapted for use with SUK-1.5 (Migliorini et al., 2011) where the control analysis at 1.5 km resolution is determined with a preliminary 3-D VAR system, and with latent heat and cloud nudging schemes. This VAR system uses a **B**-matrix whose formulation is suited to synoptic-scale rather than convective-scale dynamics as the Met Office does not yet have a truly convective-scale VAR system. It is hoped that the results of this work will help the development of a **B**-matrix that is appropriate for convective-scale dynamics. We assume for this paper that this preliminary system is still useful to study convective-scale forecast errors as characteristics of convective-scale forecast errors are expected to emerge as the ensemble of SUK-1.5 forecasts progresses.

Under consideration in the bulk of this work is a 24-member ensemble of 1-h SUK-1.5 forecasts, each valid at 1800 UTC 26 July 2007. This is the same ensemble as used in experiment C2E01 of Migliorini et al. (2011). We are interested in the properties of 1-h forecasts because our eventual aim is to build a variational assimilation system with a 1-h assimilation cycle at 1.5 km grid length, and such a system will need an effective formulation of 1-h forecast error covariance statistics. Inspection of external gravity waves (through domain averaged surface pressure tendencies) in 1.5 km ensemble forecasts revealed that initial imbalances have dispersed by 1 h (J.-F. Caron, personal communication 2010), meaning that spin-up effects are unlikely to affect our results. To minimize spin-up effects further, we have allowed 10 1-h cycles of this new system to pass before settling on the choice of 1800 UTC.

Figure 1 shows precipitation forecasts for the control member (the unmodified 3-D analysis, panel a) and member 6 (panel b). Both maps show heavy precipitation over North West Wales, which is present in all members. This precipitation is likely to be forced by orography. Member 6 also shows a line of precipitation running from South West England to the Midlands. This precipitation is present in about half of the ensemble members and, in contrast to the North West Wales region, is assumed to be unrelated to orographically forced convection. The forecast error covariances at points within these two regions are studied in this paper. The large region of precipitation at the far south of the domain in panel b is not studied as it is too close to the boundary.

Figure 2 shows the divergence of the horizontal wind field for the control (panel a) and member 6 (panel b) at level 10 (the approximate height and pressure of this and other levels referenced in this paper are shown in Table 1). The correspondence between the convergence features in this field (blue shading) and the precipitation in Fig. 1 is evident, especially the convergence line in South England in member 6, although there are many other regions showing convergence which have not met the conditions required for precipitation to occur (e.g. over South Wales). These fields demonstrate that the model can represent some small-scale convection processes explicitly. The crosshairs in these panels each mark a point of interest in these fields. Panels c and d show the latitude/level divergence field along the lines of constant longitude in panels a and b, respectively, showing the large (tall/thin) aspect ratio of the convergence features. The top of the convergence/divergence in panel c is deeper in the north compared to the south, where it reaches level 50 (Table 1). The top of the convergence/divergence in South England (panel d) reaches around level 30 over the crosshair. These features remain below

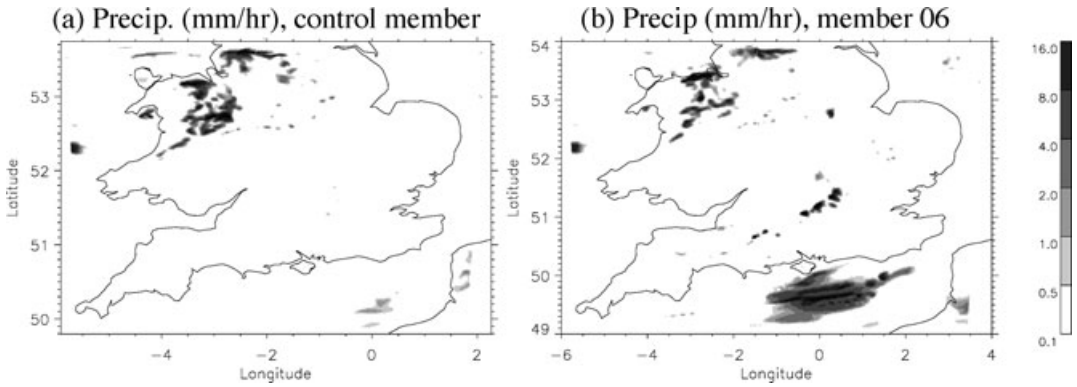

Fig. 1. Precipitation rates in two 1-h forecasts of SUK-1.5, each valid at 1800 UTC 26 July 2007. Panel a is the control forecast and panel b is one of the perturbed forecasts (member 6). Shading is to illustrate the regions of precipitation, rather than a quantitative guide. The Northwest Wales region has rates of up to 32 mm h^{-1} and the Central England region has rates of up to 8 mm h^{-1}.

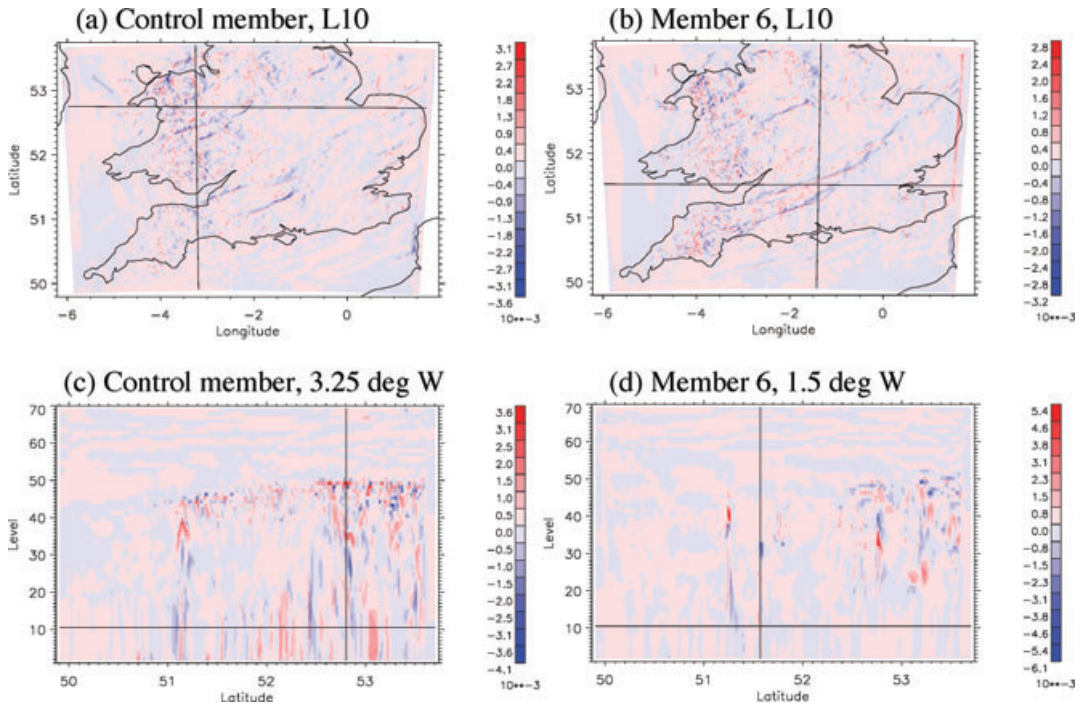

Fig. 2. Horizontal divergence fields for the control member (panels a and c) and member 6 (panels b and d) for the same situation presented in Fig. 1 at 1800 UTC. Panels a and b are for model level 10 and panels c and d are for longitudes 3.25° West and 1.5° West, respectively. Red (blue) colours indicate diverging (converging) air.

Table 1. Approximate height (above sea level) and pressure of a selection of levels in the SUK-1.5 and NAE models

Model level	Approx. height (km)	Approx. pressure (hPa)
L10 (SUK-1.5)	0.5	960
L20 (SUK-1.5)	1.4	850
L30 (SUK-1.5)	3.1	680
L34 (SUK-1.5)	4.0	605
L45 (SUK-1.5)	6.9	400
L50 (SUK-1.5)	8.5	310
L60 (SUK-1.5)	14.8	110
L13 (NAE)	3.3	690

the tropopause, which is positioned at about level 60. Patterns of vorticity (not shown) have a close correspondence with those of divergence at small scales indicating a break down in mass/wind balance expected by a scale analysis of the equations of motion (see Section 6). The specific humidity fields (not shown) are, as expected, found to be higher locally above regions of convection compared to the immediate surroundings at the same model level (e.g. at level 30, values are $0.004\,\mathrm{mg\,kg^{-1}}$ compared to $0.002\,\mathrm{mg\,kg^{-1}}$).

The latitude slices used in Fig. 2 are used throughout this paper to illustrate some of the error statistics of this run of the SUK-1.5 model.

3. Variance of forecast errors in SUK-1.5

The forecast error variance field for a given quantity and position is the mean square error of the forecast, Σ^2, where Σ is the standard deviation field. Knowledge of the error variances is important for data assimilation as Σ^2 specifies how well the a priori forecast is known at different locations. Formally Σ^2 modulates the analysis increments such that increments for quantities and regions with a high variance are generally larger than those with a small variance. Hence a mis-specification of the variances in a data assimilation system by, for example, underestimating their values, will result in the system unable to correct the a priori data adequately since it has put anomalously high trust in the a priori. In this section we show a selection of ensemble-derived variances, which we consider to be an estimate of the lower bound of the actual forecast uncertainty (a lower bound because we have not considered model error).

Figure 3 shows a selection of latitude/level cross-sections of variances of various quantities. Most VAR systems attempt to decompose the fields into components representing different physical mechanisms operating in the atmosphere (e.g. rotational modes and divergent modes) before computing their variances, for example, Parrish and Derber (1992). Panels a and b of Fig. 3 are for streamfunction (ψ) and velocity potential (χ), respectively, which are control parameters in basic versions of the Met Office VAR system. They are shown along the same latitude cross-section shown in Fig. 2(c), so the latitudinal slope of the

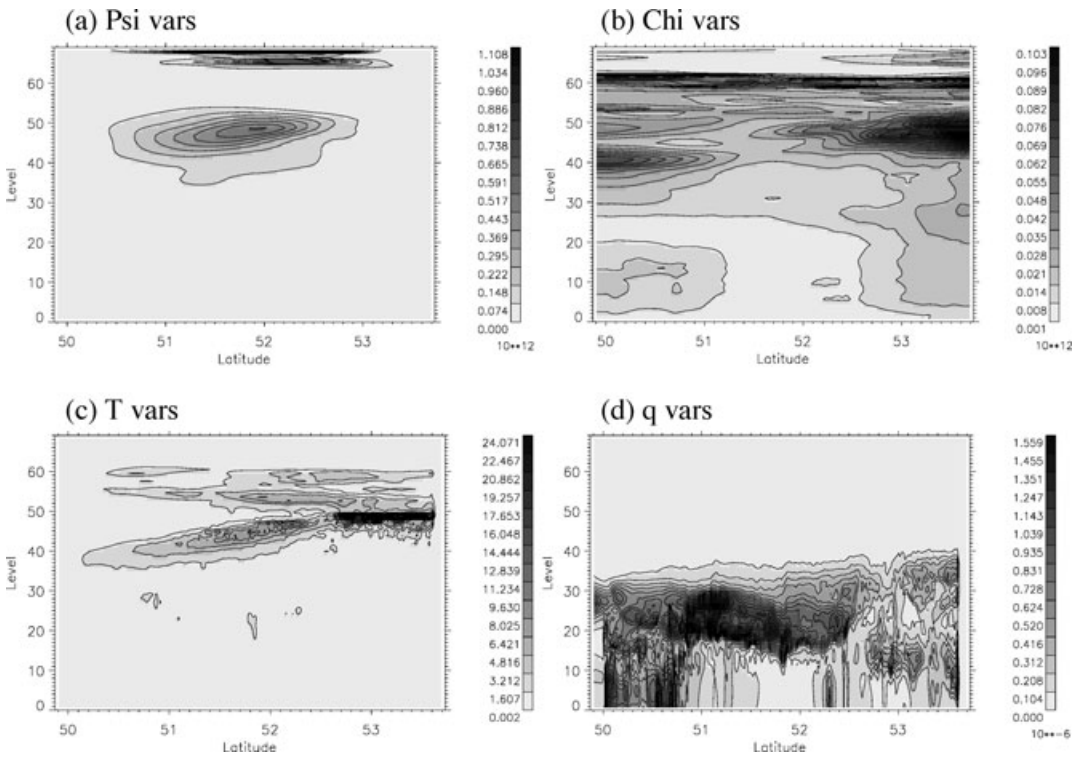

Fig. 3. Variances of streamfunction (ψ' in $m^4\,s^{-2}$), velocity potential (χ' in $m^4\,s^{-2}$), temperature (T' in K^2) and specific humidity (q' in $kg^2\,kg^{-2}$) found from an ensemble of SUK-1.5 forecasts valid at the same time and longitude as shown in Fig. 2(c).

divergence feature in that figure, for example, can be compared to features in the variance fields. The comparison is made to give a glimpse of the flow dependence of the ensemble-derived variances.

The streamfunction error, ψ', describes the rotational wind error ($\zeta'_z = \nabla_z^2 \psi'$, where ζ'_z is the vertical component of vorticity error and ∇_z^2 is the horizontal Laplacian) and is used by the Met Office as the leading (or 'Rossby-mode') control variable in VAR, Ingleby (2001). The horizontal rotational wind errors (subscript 'r') are found from ψ' as follows: $u'_r = -\partial\psi'/\partial y$ and $v'_r = \partial\psi'/\partial x$ (where x and y are distances in the longitudinal and latitudinal directions, respectively) with the condition that wind errors do not contribute to flow into or out of the LAM domain. This leads to the boundary condition of $\psi' = \text{constant}\ (=0)$ at the edge of the domain, which is also the condition imposed by the control variable transform in the Met Office VAR system. The variances of ψ' at 1800 UTC (panel a) peak at a model level that increases with latitude (about level 45 at the southern end to level 50 at the northern end). The slope of this feature reflects the basic ψ field (not shown). This feature (apart from its diminishing strength towards the lateral boundaries, which is a consequence of the LAM and the boundary conditions) corresponds to the jet in the upper troposphere. A similar feature is seen in the pressure error variances (not shown), which indicates a strong large-scale mass wind balance at these levels (a conclusion supported by the balance analysis in Section 6.1). The variance fields change only slightly from cycle to cycle. In the previous 1-h forecast valid at 1700 UTC for instance, the peak in ψ does not slope with latitude, but the basic structure of the variance field remains (not shown).

The velocity potential error, χ', describes the horizontal divergent wind error ($\delta' = \nabla_z^2 \chi'$, where δ' is the horizontal divergence error) and is used as another control variable in VAR by the Met Office. The horizontal divergent wind errors (subscript 'd') are found from χ' as follows: $u'_d = \partial\chi'/\partial x$ and $v'_d = \partial\chi'/\partial y$, again with the condition of zero flow in/out of the domain. This leads to the boundary condition of zero normal gradient of χ' at the edge of the domain, which is also the condition imposed by the control variable transform in the Met Office VAR system.

The variances of χ' at 1800 UTC (panel b) peak at levels that are similar to those where ψ' variances peak. The variances of δ' (not shown) have much finer scale structure than for the variances of χ', and peak at points in the atmosphere where δ itself is high (associated with convective activity) as in Fig. 2. This appears to be true for cycles other than at 1800 UTC, showing clear flow dependence.

Panels c and d are for temperature (T) and specific humidity (q), which are variables output directly by the model. Fluctuations in convective motion can have a significant effect on temperature due to variations in latent heating/cooling, radiative effects of cloud and adiabatic warming/cooling. Most of the variability of T' variances (panel c) appears to lie along the top of

the convection (again sloping with latitude). Specific humidity, q' is influenced by many processes, including convection which can act to hydrate the air by transporting moisture upwards and to dehydrate by precipitation and by transporting dry air downwards in downdraughts. Variances of q' are shown in panel d. There is no obvious correspondence between the presence or not of convective motion (see Fig. 2c) and q' variance features. South of 50.7° the variances in q' are fairly uniform up to level 30 or so where there is little or no convection, and more patchy variance fields elsewhere, but this apparent correspondence between q' variance and convection is not seen in other cross sections. Variances above level 30 diminish because of the rapid decrease of the specific humidity field itself with height.

Generally the factors affecting variance statistics include the dynamics of the model during the latest forecast, and the historical evolution of the ensemble, including the observation network in the last and previous ETKF (Ensemble Transform Kalman Filter) cycles. The complicated nature of these variances highlights the need for flow-dependent information to be made available for the data assimilation and an ensemble is shown to be a useful source of this information.

4. Structure and correlation functions in the SUK-1.5 and NAE models

Structure and correlation functions for forecast errors are the 3-D fields of covariance and correlation between forecast perturbations at each point in one field with perturbations at a reference point of a reference field. They are a useful way to illustrate the structure of forecast error statistics. Let $\mathbf{P}^{\mathrm{f}}(\nu_1'(\mathbf{r}_1),\ \nu_0'(\mathbf{r}_0))$ and $\mathbf{C}^{\mathrm{f}}(\nu_1'(\mathbf{r}_1),\ \nu_0'(\mathbf{r}_0))$ be the sample covariance and sample correlation, respectively, between the error of field ν_1' at position $\mathbf{r}_1$ and the error of the reference field ν_0' at position $\mathbf{r}_0$.

$$\mathbf{P}^{\mathrm{f}}(\nu_1'(\mathbf{r}_1),\ \nu_0'(\mathbf{r}_0)) = \langle \nu_1'(\mathbf{r}_1)\nu_0'(\mathbf{r}_0)\rangle = \frac{1}{N-1}\sum_{i=1}^{N}\nu_1'(\mathbf{r}_1)\nu_0'(\mathbf{r}_0),$$

$$\mathbf{C}^{\mathrm{f}}(\nu_1'(\mathbf{r}_1),\ \nu_0'(\mathbf{r}_0)) = \frac{\mathbf{P}^{\mathrm{f}}(\nu_1'(\mathbf{r}_1),\ \nu_0'(\mathbf{r}_0))}{\Sigma(\nu_1',\mathbf{r}_1)\Sigma(\nu_0',\mathbf{r}_0)}, \qquad (1)$$

where ν_i' represents a field that can be derived from model variables (u', v', p', θ', q', etc.), the angled brackets indicate average (in this case over the $N = 24$ ensemble members) and $\Sigma(\nu_i', \mathbf{r}_i)$ is the standard deviation of $\nu_i'(\mathbf{r}_i)$. Most of this work is concerned with $\mathbf{C}^{\mathrm{f}}$. The primed notation indicates a perturbation (or error) with respect to the ensemble mean, which is itself taken to be a proxy for the truth for the purpose of computing the statistics. By fixing ν_0' and $\mathbf{r}_0$, $\mathbf{P}^{\mathrm{f}}$ and $\mathbf{C}^{\mathrm{f}}$ give the 'structure' and 'correlation' functions, respectively.

Structure functions are useful because they can be compared to the analysis increment field (analysis minus background forecast) from the assimilation of a single observation of the reference field made at the reference point, for example, Dance (2004). The analysis increment field is proportional to the column of the **B**-matrix corresponding to the observation's location and so such a comparison allows the conventional **B**-matrix used in the data assimilation to be compared to the flow-dependent $\mathbf{P}^{\mathrm{f}}$-matrix derived from the ensemble. Since standard deviations are always positive, the structure function patterns are found to be similar to the correlation function patterns, especially in horizontal plots of fields where Σ does not vary strongly with horizontal position. Correlation functions are easier to plot than covariance functions (the former are always bounded between ± 1), so in the following subsections, the analysis increments that emerge from single observation experiments in VAR are compared with ensemble-derived correlation functions.

4.1. Structure and correlation functions in NAE

Before proceeding to analyse correlation functions from SUK-1.5, we first demonstrate that a 24-member ensemble is capable of revealing a signal in the correlation functions that reflects known relationships between the variables. Forecasts at 24 km resolution over the NAE domain are expected to obey near geostrophic balance since this model represents the relevant scales at the mid-latitudes, so this model is used to test whether 24 members can show a geostrophic signal.

The left panels of Fig. 4 show ensemble-derived correlation functions for 12-h NAE forecast perturbations of $p'(\mathbf{r}_1)$, $u'(\mathbf{r}_1)$ and $v'(\mathbf{r}_1)$ associated with a reference perturbation in pressure at the cross (at $\mathbf{r}_0$) near the middle of the domain at level 13 (Table 1). The right panels of Fig. 4 are the corresponding analysis increments from a VAR run with a conventional **B**-matrix on the NAE domain with a pseudo observation of pressure at the cross position. The **B**-matrix for the NAE is static, has been tuned for 6-h forecast errors and gives rise to nearly homogeneous structure functions. If the 24-member ensemble is adequate to show geostrophically related correlation signals (and assuming that the VAR **B**-matrix is an appropriate representation of forecast errors in this model) then the two sets of patterns should share common features (but the actual values need not agree).

The large-scale pressure pattern (panel a) has a region of strong positive correlation in agreement with the pressure analysis increment (panel b), but there are regions of strong anti-correlation either side (north and south) in panel a, which do not appear in panel b. The correlations of zonal and meridional winds with pressure (panels c and e, respectively) each have dipole structures associated with anti-cyclonic motion about the reference point. These features are present in the analysis increments (panels d and f), and are the well-known geostrophically balanced response to the pressure (e.g. Bartello and Mitchell, 1992; Kalnay, 2002). The correlation plots do show longer length-scales than the analysis increments, which may be explained by the longer range of the NAE forecasts (12 h) compared to the **B**-matrix statistics (tuned for 6 h).

The patterns that emerge in the left-hand panels of Fig. 4 do resemble those in the right-hand panel, but are subject to

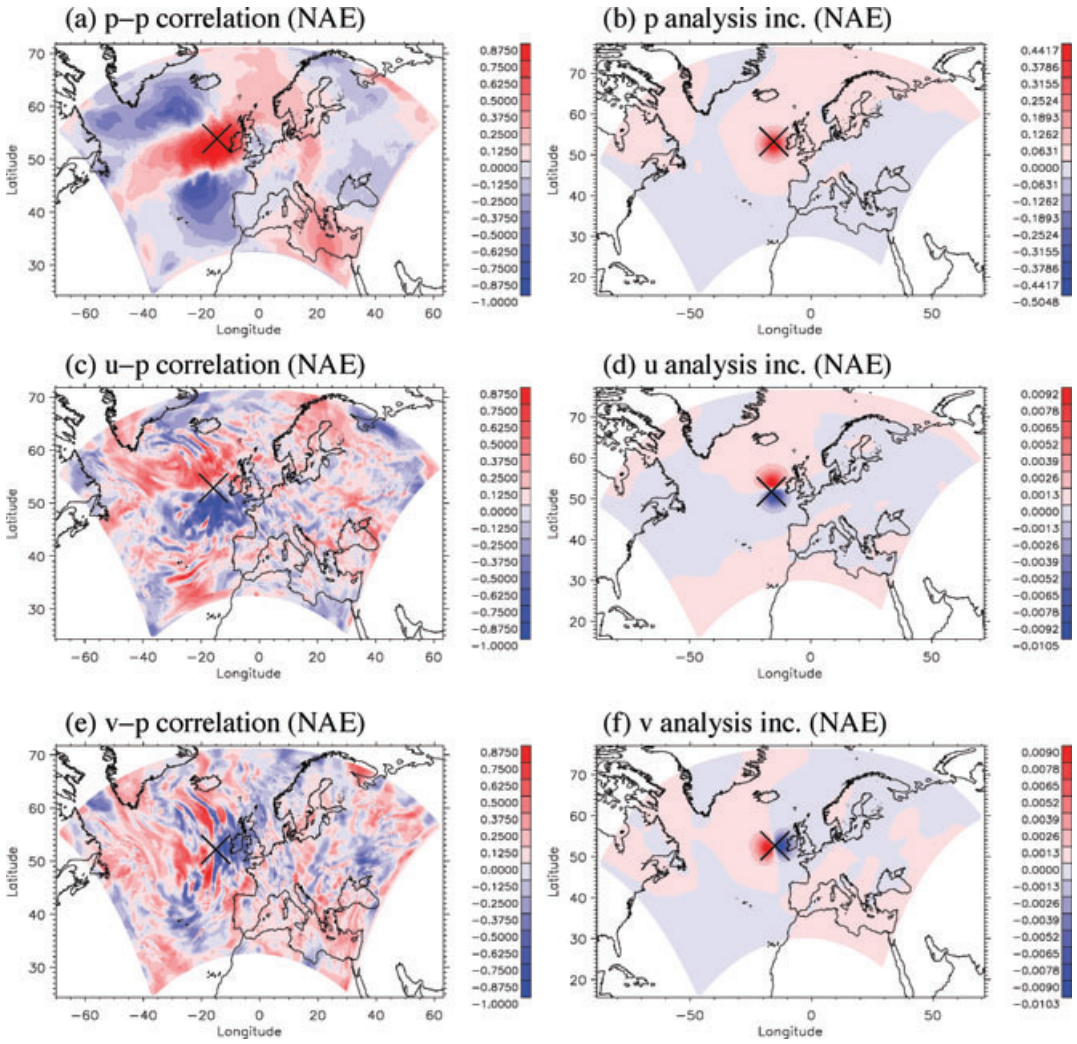

Fig. 4. Left-hand panels: correlation functions of (a) pressure, (c) zonal wind and (e) meridional wind with pressure (at the cross position) calculated from an ensemble of 12-h NAE forecasts. Right-hand panels: VAR analysis increments of the same quantities for the NAE (tuned for 6-h forecast errors) due to the assimilation of a single pressure observation (at the cross position). Results are for level 13 of the NAE and red (blue) colours indicate positive (negative) values.

noise. To study how the level of noise changes as the number of ensemble members changes, Fig. 5 shows ensemble-derived correlations at lines through the cross in Fig. 4. Cases of 5, 15 and all 24 members are shown together with theoretical results as described in the caption. The correlations for pressure with latitude (panel a), zonal wind with latitude (panel b) and meridional wind with longitude (panel c) all show evidence of less noise as the number of ensemble members increases (as expected). Results appear to settle roughly towards the broad structure of the theoretical curves (i.e. the 15- and 24-member curves). This includes the lobes in panels b and c (cf. Figs. 4c and e, respectively). Since the broad structures found in Fig. 5 appear to be robust against changes in the number of ensemble members (as only the level of noise appears to change), we consider the results found from a 24-member ensemble a reasonable indicator of the broad structure of forecast error correlations.

4.2. *Structure and correlation functions in SUK-1.5*

Figure 6 is the analogue of Fig. 4 but for the finer SUK-1.5 model, and for 1-h forecasts. The correlation results shown in panels c and e for u' and v', respectively, still show the characteristics of geostrophic balance over the domain scale [as highlighted by the VAR analysis increments (corresponding right-hand panels) which arise from the **B**-matrix used which is formulated with near geostrophic balance built-in]. This shows that this model has a domain large enough for geostrophy to still be important. From these pictures, however, it is not possible to assess how important geostrophic balance is at the small scales since, for

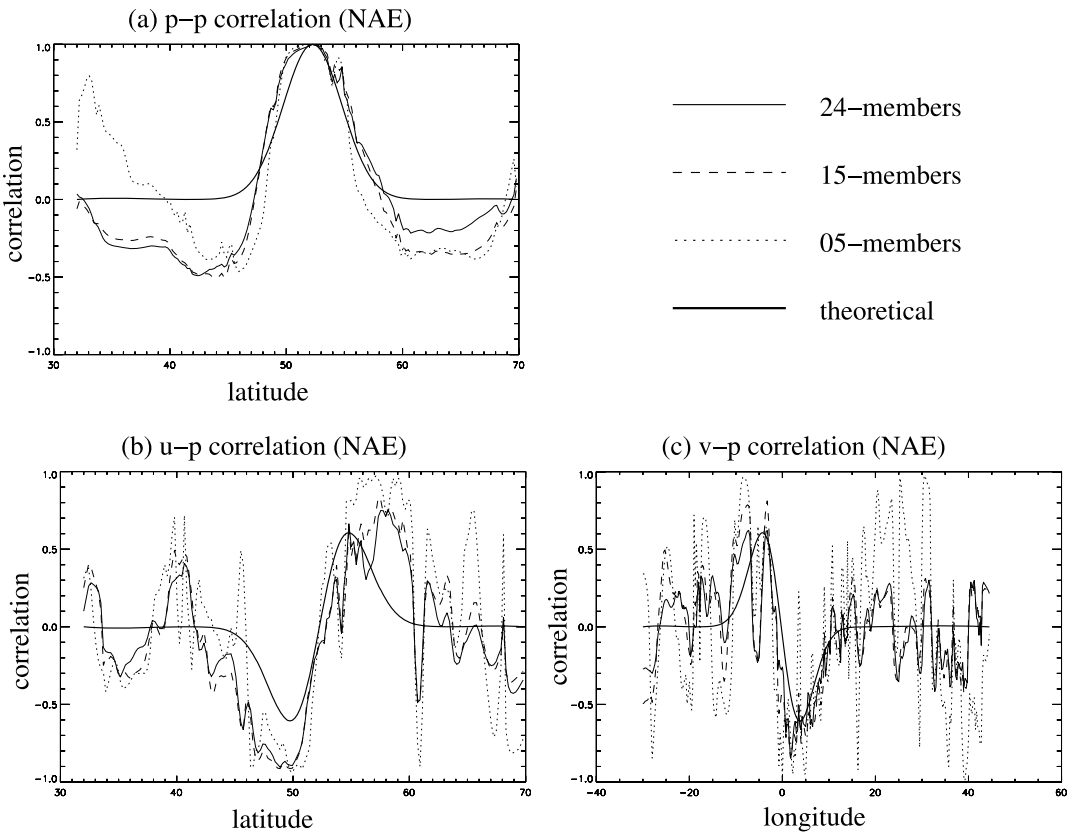

Fig. 5. Correlation functions of (a) pressure and (b) zonal wind as a function of latitude and (c) meridional wind as a function of longitude. All plots are on level 13 and through the cross in Fig. 4. Correlations are with pressure at the position of the cross in that figure and have been calculated with 5, 15 and 24 members according to the key. Theoretical curves have also been added on the basis that pressure correlations have a horizontal lengthscale of 290 km and the wind correlations are found from geostrophic balance in the way described in Kalnay (2002).

example, it is impossible to distinguish between real small-scale features and artefacts due to sampling noise. We return to this issue in Section 6 where we use a more quantitative approach to look at balances.

The VAR analysis increments are forced with zero boundary conditions on all boundaries for p' and θ', on the east and west boundaries for u', and on the north and south boundaries for v'. This is done in VAR for practical reasons (e.g. for consistency with the larger scale driving model at the lateral boundaries), but the comparison with the correlation results does suggest that this does change the correlation lengthscales artificially (e.g. comparing p' responses in panels a and b).

Figure 7 is similar to Fig. 6 but for θ' (correlated with p' at the cross position) where panels a and b are for level 30 and panels c and d are for the latitude/level cross sections through longitude of the cross (at $\mathbf{r}_0$). Panels a and b both show a large-scale correlation in θ' (still due to the p' perturbation at the position of the cross), but the signs disagree. Panels c and d each show vertical bands of alternating sign in the correlation between $\theta'(\mathbf{r}_1)$ and $p'(\mathbf{r}_0)$, but the signs disagree roughly in a systematic way. The VAR increments diagnose θ' from p' in the following way, ignoring the secondary effect of moisture increments as in Bannister (2008b):

$$\theta' = \left[\frac{g\kappa}{c_p} \Pi_0 \left(\frac{\partial \Pi_0}{\partial z} \right)^{-2} \frac{\partial}{\partial z} - \frac{g\kappa}{c_p} \left(\frac{\partial \Pi_0}{\partial z} \right)^{-1} - \kappa\theta_0 \right] p'/p_0, \tag{2}$$

where g is the acceleration due to gravity, $\kappa = c_p/c_v$, c_p and c_v are the isobaric and isochoric specific heat capacities of air, Π is Exner pressure, z is height and variables with subscript 0 are reference state quantities rather than perturbations. Equation (2) relates increments p' and θ' due to hydrostatic balance. The disagreement, especially with regard to the signs between panels a and b, and c and d, suggest that hydrostatic balance is not obeyed in SUK-1.5 in this cross section. It is unlikely that the difference can be explained in terms of sampling error. First, the ensemble result appears strong and of the wrong sign, and second, the ensemble is capable of producing a result like panel d at some points in other cross sections, which are not associated with rainfall (not shown), suggesting hydrostatic balance is satisfied in some places. Similar patterns to that shown in panel c are found also in correlations derived from a lower resolution ensemble over the NAE domain (not shown). We investigate hydrostatic balance further in Section 6.2.

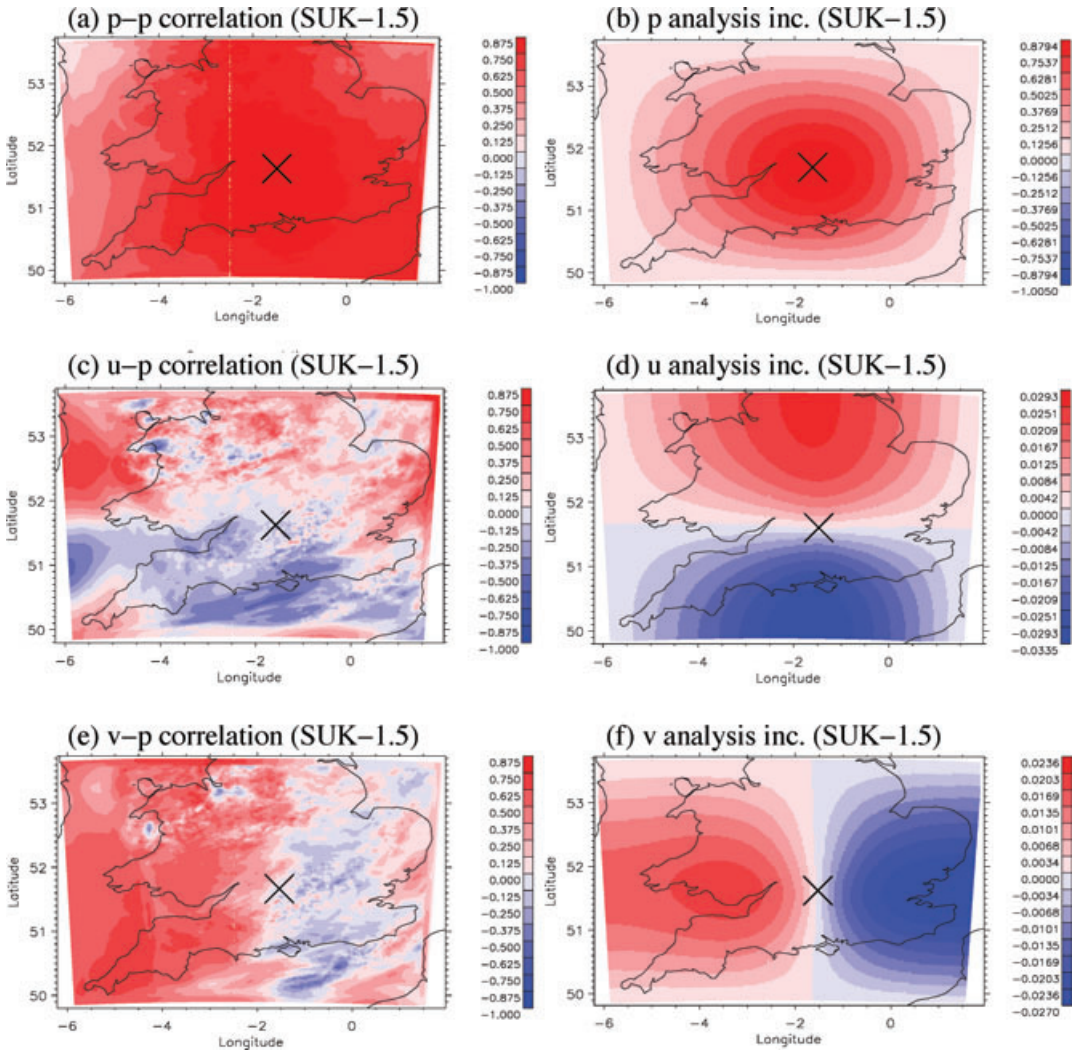

Fig. 6. Left-hand panels: correlation functions of (a) pressure, (c) zonal wind and (e) meridional wind with pressure (at the cross position) calculated from an ensemble of 1-h SUK-1.5 forecasts. Right-hand panels: high-resolution VAR analysis increments of the same quantities (tuned for 1-h forecast errors) due to the assimilation of a single pressure observation (at the cross position). All panels are for level 30 of SUK-1.5 and red (blue) colours indicate positive (negative) values.

5. Correlation statistics in vertical cross sections in SUK-1.5

The correlation and structure functions shown in the last section are concerned with 3-D fields correlated to a fixed reference position, $\mathbf{r}_0$. In this section we allow $\mathbf{r}_0$ to vary to give a selection of ensemble-derived forecast error correlation statistics for SUK-1.5.

5.1. Point-by-point (local) correlation functions in SUK-1.5

A selection of point-by-point correlations are plotted in Fig. 8 [point-by-point correlations are where $\mathbf{r}_0 = \mathbf{r}_1$ in (1)]. The local correlations between streamfunction and pressure errors, $\mathbf{C}^{\mathrm{f}}(\psi'(\mathbf{r}_1),\ p'(\mathbf{r}_1))$ provide a rough guide to the degree of geostrophic balance (panel a). This shows strong correlation throughout the troposphere, especially in the upper troposphere. The thickness of the layer where the correlation is positive and very close to unity around level 50 (Table 1) is thinner above convection, which is unsurprising as the Brunt-Väisälä frequency, and hence gravity wave speed, is likely to be smaller close to rather than away from convecting regions resulting in a slower rate of geostrophic adjustment. Fourier transforming the ensemble members and computing the same correlations, but as a function of total horizontal wavenumber and level (panel b) shows that only the smallest wavenumbers ($<0.0001\,\mathrm{m}^{-1}$), or equivalently the largest lengthscales ($>50\,\mathrm{km}$) (note the lengthscale axis above the spectral plots) are responsible for the height dependence in panel a as the correlations are very weak for

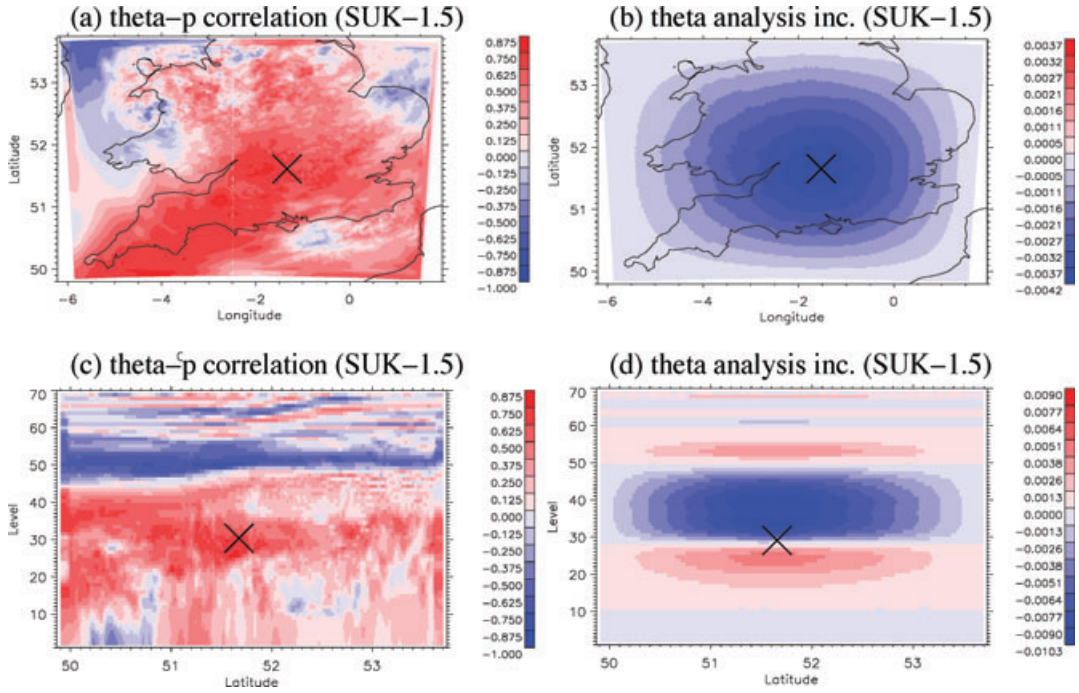

Fig. 7. Left-hand panels: correlation functions of potential temperature with pressure (at the cross position) calculated from an ensemble of 1-h SUK-1.5 forecasts. Right-hand panels: high-resolution VAR analysis increments of potential temperature (tuned for 1-h forecast errors) due to the assimilation of a single pressure observation (at the cross position). The top panels are for level 30 of SUK-1.5 and the bottom panels are for the cross section at constant longitude through the cross position and red (blue) colours indicate positive (negative) values.

most of the spectral space shown. A more targeted analysis of geostrophic balance is given in Section 6.1.

The forecast error covariance formulations used in earlier versions of VAR systems were often based on the assumption that the correlations between rotational and divergent wind errors, $\mathbf{C}^{\mathrm{f}}(\psi'(\mathbf{r}_1), \chi'(\mathbf{r}_1))$, are zero, Bannister (2008b). The local correlations between ψ' and χ' are shown in panel c, which shows that this assumption is not good in this system (although it is rarely found to be well satisfied, e.g. Bannister et al., 2008). By averaging additionally over longitude, as well as over ensemble member (to reduce sampling noise), a similar picture to panel c emerges, but with slightly reduced correlations at middle tropospheric levels. The wavenumber dependence of this correlation (panel d) shows no strong dependence on the range of scales of motion represented in SUK1.5, indicating that this assumption made by VAR is poor at all scales.

5.2. *Vertical correlation functions in SUK-1.5*

In this subsection, the reference point of the correlations ($\mathbf{r}_0$ in eq. 1) varies in the horizontal, and $\mathbf{r}_1$ is forced to have the same horizontal position as $\mathbf{r}_0$, but is allowed to have a variable height (analogous correlations are also found as a function of total horizontal wavenumber whereby the error fields are first Fourier transformed). Correlations plotted in this way show the vertical structure of correlations as a function of position (or wavenumber). Figures 9 and 10 show vertical correlations between a selection of pairs of perturbations where $\mathbf{r}_0$ is fixed at level 30. The left-hand panels show correlations as a function of latitude (at the particular longitude of Fig. 2c), and the right-hand panels as a function of wavenumber.

The vertical correlations of θ' with p' at level 30 (Table 1) vary with latitude (panel a of Fig. 9) in a similar way to that shown in Fig. 7(c) (where the source point is fixed at the position of the cross). This similarity is not surprising as the horizontal pressure correlations between that fixed point and all other points on level 30 (Fig. 6a) are strong, so the response in Fig. 7(c) is as though the reference point is everywhere on that level. The basic vertical structure of the correlations does not change significantly with wavenumber (panel b), which shows positive correlations up to level 50 and a band of negative correlations above this. There is evidence of a change of sign in correlation at some small wavenumbers from positive below level 30 to negative above this level. This is similar to the hydrostatic response expected around level 30 (cf. Fig. 7d each side of level 30). Additionally the positive correlations do strengthen with increasing wavenumber. This is an example of the changing nature of the tropospheric flow regime to one where the aspect ratio becomes larger at smaller horizontal scales (a large aspect ratio means that large vertical scales are associated with small horizontal scales). The transition to this new regime starts around wavenumber 0.0006 m^{-1} (equivalent to 10 km lengthscale). This

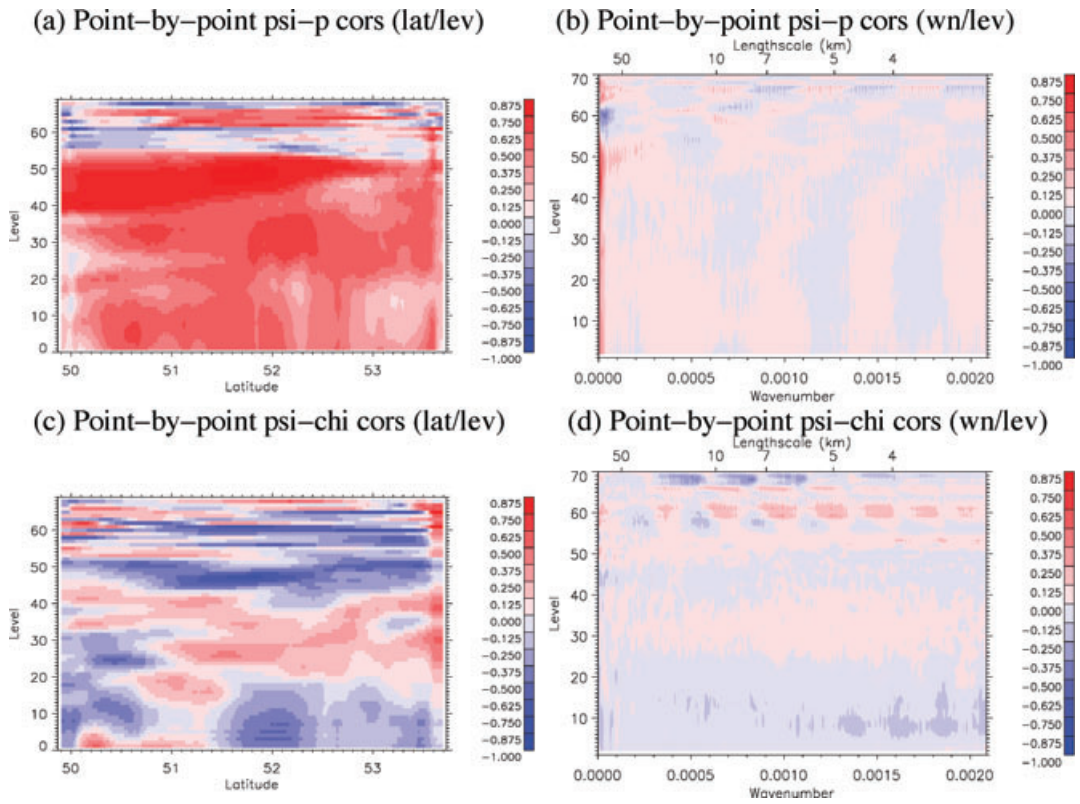

Fig. 8. Correlation between ψ' and p' (panels a and b) and between ψ' and χ' (panels c and d) computed on a point-by-point basis in latitude space at the same longitude as shown in Fig. 2(c) (left-hand panels) and in spectral space (right-hand panels). Red (blue) colours indicate positive (negative) correlations. Note that lengthscale axes are given at the top of the wavenumber plots.

feature, which has not to our knowledge been shown in previous studies (as previous models have been too coarse, e.g. Berre, 2000, which had a lower scale limit of 10 km), will be studied in later work by investigating how it can be reproduced with alternative hypotheses to those currently used in background error covariance schemes for synoptic scales.

The vertical correlations for χ' with itself show no major structural changes with latitude (panel c). The 3-D isotropy (3-D isotropy is where large vertical scales are associated with large horizontal scales) is preserved over all wavenumbers considered (panel d) for this variable, even when the convective-scale regime shows up in other variables. This behaviour is seen over all lengthscales considered in other studies, e.g. Berre (2000) and Ingleby (2001).

The vertical correlations of θ' with itself (panel a of Fig. 10) show evidence of structures with larger aspect ratio at latitudes north of 52.3° than south of this latitude. This is the region where most of the convection is occurring along this cross section (see Fig. 2c). This effect shows up in the wavenumber dependence (panel b). This shows the large-scale 3-D isotropy signature (as found in χ' autocorrelations above), but here only down to horizontal lengthscales of about 10 km. At smaller horizontal lengthscales the vertical lengthscales increase and the band of negative correlations in the upper troposphere strengthen. This has potentially important consequences for convective-scale data assimilation as it means, for example, that high-resolution satellite measurements of T in the upper troposphere may contain important information about T in the lower parts of the troposphere. This link can be exploited only if this effect is represented in the background error covariances used in the data assimilation. A similar picture is seen in the vertical correlations of q' with itself (panels c and d) apart from, in this case, there is no band of negative correlations above level 50.

6. Balance diagnostics in SUK-1.5

A scale analysis of the momentum equations reveals that linear balance (essentially geostrophic balance) is expected to hold for small Rossby number (Ro) and hydrostatic balance is expected to hold for small Ro $\times$ W/U, where Ro $= U/(Lf)$ is the Rossby number, U is the characteristic horizontal flow speed, W is the characteristics vertical flow speed, L is the horizontal lengthscale and f is the Coriolis parameter, see for example, section 11.4.2 of Salby (1996). Both kinds of balance are important to conventional forecast error covariance modelling in VAR (e.g. Bannister, 2008b), but are expected to break down to

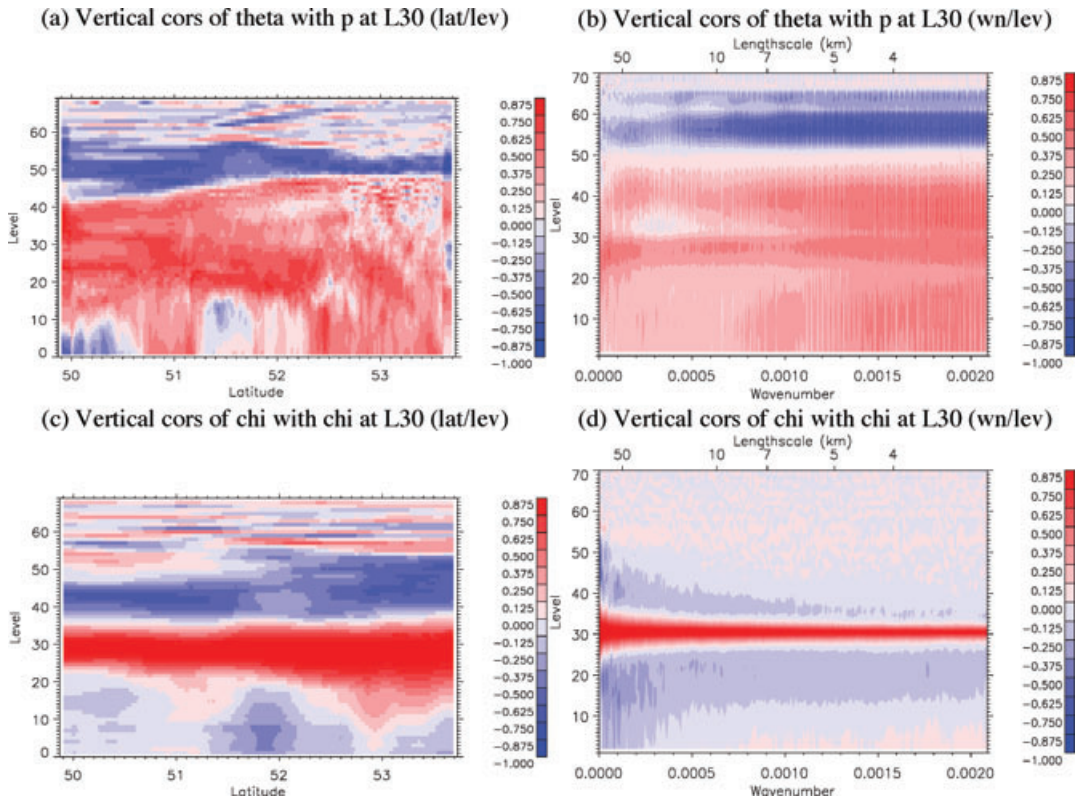

Fig. 9. Vertical correlations with level 30 between θ' and p' (panels a and b) and χ' and itself (panels c and d) computed in latitude space at the same longitude as shown in Fig. 2(c) (left-hand panels) and in spectral space (right-hand panels). Red (blue) colours indicate positive (negative) correlations. Note that lengthscale axes are given at the top of the wavenumber plots.

some extent as the scale of the motion reduces, as is possible in high-resolution models. In this section we try to diagnose at what scales the geostrophic and hydrostatic balances are found to break down, if at all, in the SUK-1.5 forecasts according to our balance diagnostics described below. This is an important aspect to determine as it will provide a guide on the scales below which a new approach to forecast error covariance modelling will be required in data assimilation.

6.1. Linear balance diagnostic

The starting point for the linear balance diagnostic are the horizontal momentum equations of the dynamical core of the Met Office model in Davies et al. (2005) from which the equation for horizontal divergence, δ is derived. The result is linearized with respect to the ensemble mean giving a mass part, $\mathcal{M}'$, a wind part, $\mathcal{W}'$ and other terms, as follows:

$$\frac{D\delta'}{Dt} = \mathcal{M}' + \mathcal{W}' + \text{horiz. Coriolis} + \text{metric terms} + \text{forcing} + \text{other terms}, \tag{3}$$

where

$$\mathcal{M}' = c_p\theta_{v0}\left(\frac{\partial^2\Pi'}{\partial x^2}\right)_z + c_p\theta_{v0}\left(\frac{\partial^2\Pi'}{\partial y^2}\right)_z + c_p\left(\frac{\partial^2\Pi_0}{\partial x^2}\right)_z\theta_v' + c_p\left(\frac{\partial^2\Pi_0}{\partial y^2}\right)_z\theta_v', \tag{4}$$

and

$$\mathcal{W}' = -f\left(\frac{\partial v'}{\partial x}\right)_z + f\left(\frac{\partial u'}{\partial y}\right)_z - \frac{\partial f}{\partial x}v' + \frac{\partial f}{\partial y}u'. \tag{5}$$

In these expressions, D/Dt is the Lagrangian derivative, u, v, θ_v and Π are zonal wind, meridional wind, virtual potential temperature and Exner pressure, respectively, subscript 0 indicates the ensemble mean and a prime indicates deviation from this mean (both are functions of position). Horizontal derivatives are performed on a constant height level (indicated by the subscript z), where we use the following relations with the derivatives on constant model level (subscript η): $(\partial\gamma/\partial\chi)_z \approx (\partial\gamma/\partial\chi)_\eta - (\partial z/\partial\chi)_\eta(\partial\gamma/\partial z)$ and $(\partial^2\gamma/\partial\chi^2)_z \approx (\partial^2\gamma/\partial\chi^2)_\eta - 2(\partial z/\partial\chi)_\eta(\partial^2\gamma/\partial z\,\partial\chi)_\eta + (\partial z/\partial\chi)_\eta^2(\partial^2\gamma/\partial z^2)$, where γ is a model quantity and χ is either x or y. Note that the $\partial f/\partial x$ term is present in (3) to account for a rotated grid where x and y may not necessarily correspond to longitude and latitude, respectively.

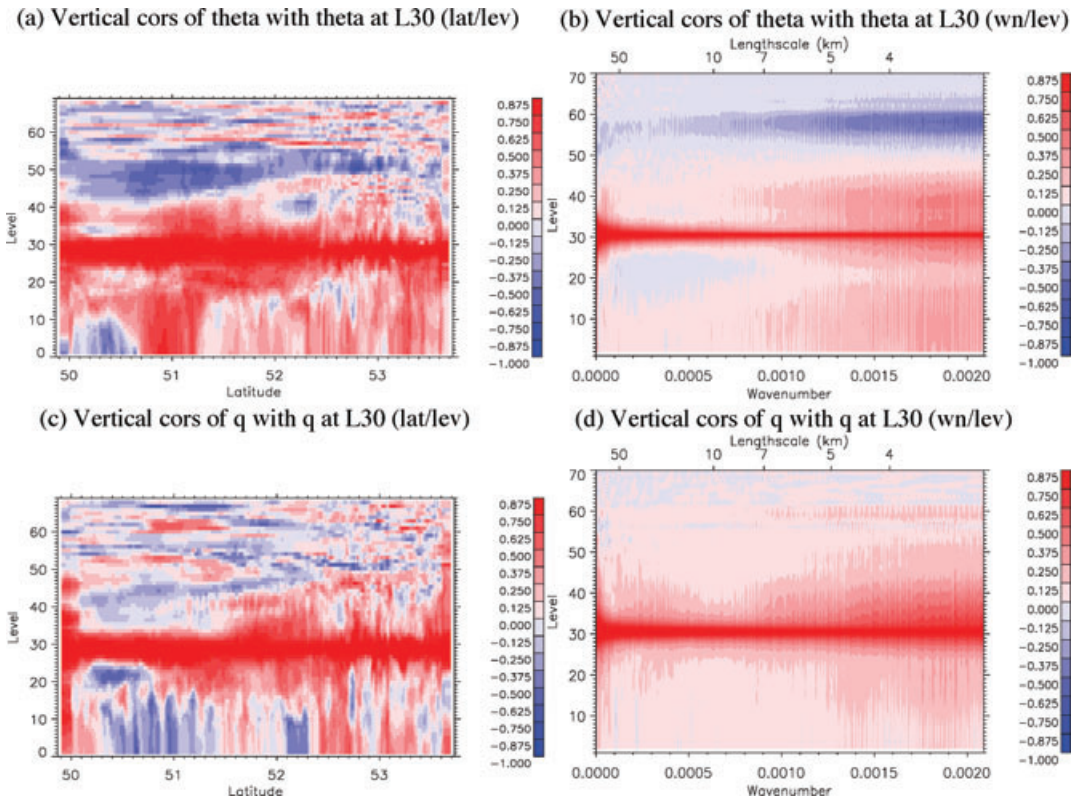

Fig. 10. Vertical correlations with level 30 between θ' and itself (panels a and b) and q' and itself (panels c and d) computed in latitude space at the same longitude as shown in Fig. 2(c) (left-hand panels) and in spectral space (right-hand panels). Red (blue) colours indicate positive (negative) correlations. Note that lengthscale axes are given at the top of the wavenumber plots.

The values $\mathcal{M}'$ and $\mathcal{W}'$ are computed for each ensemble member and the correlation between them (over the ensemble) is found. Linear balance is then assumed to hold if these two quantities are strongly anti-correlated on the basis that if other terms (especially $D\delta/Dt$) vary with a comparable magnitude then the strong anti-correlation will be lost. Figure 11 (a) shows correlation between $\mathcal{M}'$ and $\mathcal{W}'$ averaged over all latitudes for the longitude corresponding to that shown in Fig. 2(c) and for three model levels. The effective resolutions of the ensemble fields are first degraded to have different effective grid sizes from 0 (no degradation) to 100 (meaning the members have been averaged over surrounding points extending 100 grid boxes in each direction making the effective grid length 150 km). This allows us to explore the relevance of linear balance at different effective scales. The two levels shown that are inside the troposphere—levels 20 (continuous line) and 45 (dotted line)—show a general strengthening (correlation $\rightarrow -1$) of the mass-wind anti-correlation with increasing scale. Level 20 does show a slight decrease of the anti-correlation above 65×1.5 km effective grid size, which we assume is due to imbalance introduced by sampling over regions affected by orography. Level 45, however, is less susceptible to this effect and behaves in the expected way. Level 60 lies close to the tropopause and is inherently unbalanced, as found in global models (Ingleby, 2001). Approximate heights and pressures of these levels are shown in Table 1.

According to this diagnostic there is no effective grid size where there is a sudden change in mass-wind balance. Note that the anti-correlation of -0.5 for level 45 corresponds to to 50×1.5 km, which indicates that, at horizontal scales below 75 km, geostrophic balance becomes less important. This is not dissimilar to the result of Berre (2000) who looked at mass and vorticity correlations of spectral modes of ALADIN forecasts, even though Berre used a population of differences between 36- and 12-h forecasts rather than from an ensemble.

6.2. *Hydrostatic balance diagnostic*

A similar diagnostic can be composed to estimate the degree of hydrostatic balance. The vertical wind (w') equation from Davies et al. (2005) is the relevant equation to look at hydrostatic balance. In linearized form this is

$$\frac{Dw'}{Dt} = \mathcal{P}' + \mathcal{T}' + g + \text{Coriolis} + \text{metric terms} + \text{forcing} + \text{other terms}, \quad (6)$$

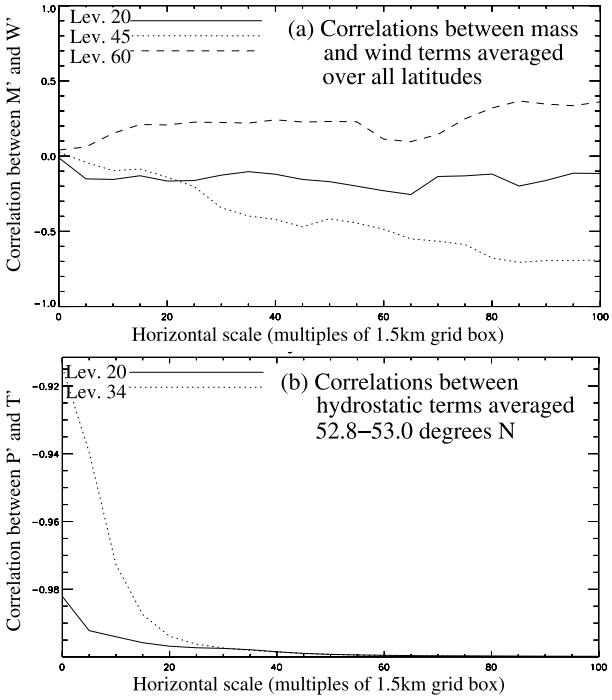

Fig. 11. Panel a: correlations between terms $\mathcal{M}'$ and $\mathcal{W}'$ in the horizontal divergence eq. (3) at three model levels (see legend) and averaged over all latitudes. Panel b: correlations between terms $\mathcal{P}'$ and $\mathcal{T}'$ in the vertical momentum eq. (6) at two model levels (see legend) and averaged between the two latitudes in the caption. In both panels data are for the longitude as that of Fig. 2(c).

where

$$\mathcal{P}' = \theta_{v0} \frac{\partial \Pi'}{\partial z}, \tag{7}$$

and

$$\mathcal{T}' = \frac{\partial \Pi_0}{\partial z} \theta_v'. \tag{8}$$

Hydrostatic balance is satisfied exactly if $0 = \mathcal{P}' + \mathcal{T}'$, which is the perturbation version of $g + c_p \theta_v \partial \Pi / \partial z = 0$, which is a more familiar form of hydrostatic balance.

In an analogous way to the mass-wind correlations, the values $\mathcal{P}'$ and $\mathcal{T}'$ have been computed for each ensemble member and the correlation between them has been found. Hydrostatic balance is then assumed to hold if these two quantities are strongly anti-correlated. Figure 11(b) shows correlation between $\mathcal{P}'$ and $\mathcal{T}'$ averaged over latitudes 52.8–53.0° for the longitude corresponding to that shown in Fig. 2(c) and for two model levels. This latitude band has been chosen because it coincides with convection. Model levels 20 (continuous line) and 34 (dotted line)—see Table 1—have been chosen because they are those that have, respectively, the maximum and minimum degree of hydrostatic balance in the latitude band. The correlations are shown as a function of the degraded resolution of the ensemble members. According to this diagnostic, there is monotonic strengthening of the degree of hydrostatic balance as the effective scale increases. This may be thought of as the averaging-out of non-hydrostatic effects over gradually larger areas. Nevertheless, the anti-correlation between $\mathcal{P}'$ and $\mathcal{T}'$ remains strong, even down to the 1.5 km grid scale (no spatial averaging) in the region of convection (note the range of correlation in Fig. 11b goes from -0.99 to -0.91). In the light of the result in panels a and c of Fig. 7 (suggesting lack of hydrostatic balance), this indicates that even anti-correlations as strong as -0.98 in this diagnostic may indicate a significant departure from hydrostatic balance. Extrapolating the curves backwards would suggests a rapid weakening of hydrostatic balance at scales much smaller than 1.5 km.

7. Discussion and conclusion

This work has served to highlight some important differences between short-range forecast error statistics at convective-scales and those at synoptic and larger scales. Until recently the scales of motion over which forecast error statistics have been studied was from global down to 10 km at the smallest. This paper uses an ensemble of forecasts made with a Met Office convection-permitting model with a 1.5 km grid length over the Southern United Kingdom to gain knowledge down to such small scales. This study is important as forecasts are thought to have different error properties at convective-scales, and these should be considered when designing a background error covariance scheme valid for variational data assimilation at these scales.

Maps of precipitation and divergence have been used to identify regions of convecting and non-convecting air and much of this study has focused on statistics within one cross section that has both types of flow.

Statistics have been derived from an ensemble of 1-h forecasts based on perturbations from the Met Office's MOGREPS ensemble prediction system adapted to work with SUK-1.5. For purposes of this work we assume that the 24 ensemble members (1 control and 23 perturbations) are representative of a probability distribution function that describes knowledge of the actual forecast error. This assumption is impossible to justify thoroughly without the availability of more members but we have attempted to show that our results remain useful. By studying univariate and multivariate correlations for the lower resolution ensemble over the NAE domain for a variable number of ensemble members (<24), we see that the results appear to settle on those found for 24 members. For the high-resolution SUK-1.5 model, we have shown results of instantaneous correlations at 1800 UTC. We have also time-averaged many of the covariance results shown in this paper over the four last ETKF 1-h forecast cycles (validity times 15, 16, 17 and 1800 UTC). We have not shown these averaged results as the important structures present in the instantaneous results remain. This adds some robustness to our results as it suggests that although noisy, 24-member

ensembles do contain signals that are likely to be physically reasonable.

The variance statistics indicate the degree of confidence in the forecasts and show signs of flow dependence. For instance T' variances peak at levels corresponding to the top of convection. The background error variances implied from the current experimental version of VAR for use with SUK-1.5, which are found from an NMC procedure (not shown), can be very different from the ensemble-derived variances, which motivates our work to develop a VAR system that has forecast error covariance statistics which are more appropriate to the high-resolution assimilation and forecasting problem.

We find that some variables, notably θ' and q', have autocorrelation functions that deviate from 3-D isotropy at the convective-scale. Large horizontal scales are associated with large vertical scales (3-D isotropy) for horizontal scales larger than about 10 km only. Below the 10 km scale, the correlation functions can have large aspect ratios, which are associated with regions of convection. Other variables, notably χ', maintain 3-D isotropy at all scales.

The domain of the SUK-1.5 model is still large enough to have scales that show a degree of geostrophic balance. This shows strong correlations between pressure and rotational wind perturbations for scales somewhat larger than 50 km throughout most of the free troposphere. An analysis of the correlation between mass and wind terms in the linear balance equation confirms this result, but does find imbalances in the stratosphere at all scales and in the boundary layer, which is affected by the surface and orography. In the free troposphere we find that geostrophic balance is significant with greater than $|-0.5|$ correlation coefficient at horizontal scales above about 75 km (a correlation of -1 indicates perfect geostrophic balance). The degree of balance reduces as the horizontal scale shortens, but our correlation diagnostic does not show a sudden drop in geostrophic balance, but is instead a gradual process.

Hydrostatic balance too is satisfied less strongly as the scale reduces, and inside convecting regions. Our correlation diagnostic for hydrostatic balance remains high, even at the grid scale and inside convection where correlations are greater than $|-0.9|$ (a correlation of -1 indicates perfect hydrostatic balance). Since the vertical correlations between p' and θ' shown in Fig. 7(c) are not characteristic of hydrostatic balance, this suggests that hydrostatic correlations very close to -1 (i.e. much stronger than $|-0.9|$) must be found to indicate that this balance is prevalent. It is difficult to calibrate this diagnostic against the existance or not of hydrostatic balance using the information that we have, but we may suggest that the scale where the two curves in Fig. 11(b) separate may indicate a breakdown of hydrostatic balance at some levels in the column. This happens at about 25 grid lengths (35 km) inside this convecting region. Vetra-Carvalho et al. (2010) compared the vertical correlations of potential temperature perturbations, $\theta' - \theta'$, with those of the 'hydrostatic potential temperature' (found from pressure perturbations through (2)), $\theta'_{\mathrm{H}} - \theta'_{\mathrm{H}}$ after degrading the resolution of the fields in a similar way as is done here. For their case study they found that the $\theta' - \theta'$ and $\theta'_{\mathrm{H}} - \theta'_{\mathrm{H}}$ correlation matrices differ at horizontal lengthscales below 20 km in convecting regions. Their and our cases are different, but the two results are in the same ballpark. This will be examined in forthcoming work in the context of high-resolution data assimilation.

All of these results have potentially significant implications for high-resolution data assimilation, which will require modification to account for the diminishing balance (especially geostrophic balance). For example, the Met Office's and others' schemes use the rotational wind as the 'master' balanced variable from which other balanced variables are derived, for example, balanced pressure. The balanced pressure is augmented with an unbalanced pressure variable. The significance of this partitioning is so that both variables (rotational wind and unbalanced pressure) are taken to be mutually uncorrelated. This relies on the property that the rotational wind describes the balanced flow, which is no longer the case given the lack of geostrophic balance at small scales. This will be studied in future work, which will consider how the diminishing balance properties potentially invalidate the existing choice of control variables and how new ones could be chosen to have convective-scale properties. It should be noted that although the effects of forecast errors at convective-scale need to be considered in high-resolution data assimilation systems, errors for the large-scale quasi-balanced flow still need to be modelled (e.g. using current methods) so that the synoptic-scale and mesoscale parts of the flow are captured realistically (as stressed in, e.g. Lean et al., 2008).

8. Acknowledgments

The contributions to this work from RNB and SM have been supported by the NERC National Centre for Earth Observation, and the contribution from MAGD has been supported by the Met Office. Calculations were performed using the Met Office's supercomputer facility in Exeter, UK. We are very grateful for the valuable comments of Dale Barker, Sue Ballard, Jean-Francois Caron and two anonymous reviewers of this paper.

References

Bannister, R. N. 2008a. A review of forecast error covariance statistics in atmospheric variational data assimilation – I: characteristics and measurements of forecast error covariances. *Q. J. R. Meteorol. Soc.* **134**, 1951–1970.

Bannister, R. N. 2008b. A review of forecast error covariance statistics in atmospheric variational data assimilation – II: modelling the forecast error covariance statistics. *Q. J. R. Meteorol. Soc.* **134**, 1971–1996.

Bannister, R. N., Katz, D., Cullen, M. J. P., Lawless, A. S. and Nichols, N. K. 2008. Modelling of forecast errors in geophysical fluid flows. *Int. J. Numer. Meth. Fluids* **56**, 1147–1153.

Bartello, P. and Mitchell, H. L. 1992. A continuous three-dimensional model of short-range forecast error covariances. *Tellus* **44A**, 217–235.

Berre, L. 2000. Estimation of synoptic and mesoscale forecast error covariances in a limited area model. *Mon. Wea. Rev.* **128**, 644–667.

Berre, L., Ştefănescu, S. E. and Pereira, M. B. 2006. The representation of the analysis effect in three error simulation techniques. *Tellus* **58A**, 196–209.

Bishop, C. H., Etherton, B. J. and Majumdar, S. J. 2001. Adaptive sampling with the ensemble transform Kalman filter – Part I: theoretical aspects. *Mon. Wea. Rev.* **129**, 420–436.

Bowler, N. E., Arribas, A., Mylne, K. R., Robertson, K. B. and Beare, S. E. 2008. The MOGREPS short-range ensemble prediction system. *Q. J. R. Meteorol. Soc.* **134**, 703–722.

Buehner, M. 2005. Ensemble derived stationary and flow dependent background error covariances: evaluation in a quasi-operational NWP setting. *Q. J. R. Meteorol. Soc.* **131**, 1013–1043.

Dance, S. L. 2004. Issues in high resolution limited area data assimilation for quantitative precipitation forecasting. *Physica D* **196**, 1–27.

Davies, T., Cullen, M. J. P., Malcolm, A. J., Mawson, M. H., Staniforth, A. and co-authors. 2005. A new dynamical core for the Met Office's global and regional modelling of the atmosphere. *Q. J. R. Meteorol. Soc.* **131**, 1759–1782.

Dixon, M. A. G., Li, Z., Lean, H., Roberts, N. and Ballard, S. 2009. Impact of data assimilation on forecasting convection over the United Kingdom using a high-resolution version of the Met Office unified model. *Mon. Wea. Rev.* **137**, 1562–1584.

Ehrendorfer, M. 2007. A review of issues in ensemble-based Kalman filtering. *Meteorol. Z.* **16**, 795–818.

Fisher, M. 2003. Background error covariance modelling. In: *ECMWF Seminar on Recent Developments in Data Assimilation for Atmosphere and Ocean*, 8–12 September 2003, ECMWF, Reading UK, 45–64.

Houtekamer, P. L. and Mitchell, H. L. 2001. A sequential ensemble Kalman filter for atmospheric data assimiltion. *Mon. Wea. Rev.* **129**, 123–137.

Ingleby, N. B. 2001. The statistical structure of forecast errors and its representation in the Met Office global 3-dimensional variational data assimilation scheme. *Q. J. R.Meteor. Soc.* **127**, 209–231.

Kalnay, E. 2002. *Atmospheric Modelling, Data Assimilation and Predictability*. Cambridge University Press, Cambridge, UK. 364 pp.

Kepert, J. D. 2009. Covariance localisation and balance in an ensemble Kalman filter. *Q. J. R. Meteorol. Soc.* **135**, 1157–1176.

Lean, H. W., Clark, P. A., Dixon, M., Roberts, N. M., Fitch, A. and co-authors. 2008. Characteristics of high-resolution versions of the Met Office unified model for forecasting convection over the United Kingdom. *Mon. Wea. Rev.* **136**, 3408–3424.

Lorenc, A. C. 2003a. Modelling of error covariances by four-dimensional variational assimilation. *Q. J. R. Meteorol. Soc.* **129**, 3167–3182.

Lorenc, A. C. 2003b. The potential of the ensemble Kalman filter for NWP: a comparison with 4d-Var. *Q. J. R. Meteorol. Soc.* **129**, 3183–3203.

Migliorini, S., Dixon, M. A. G., Bannister, R. N. and Ballard, S. P. 2011. Ensemble prediction for nowcasting with a convection-permitting model – Part I: description of the system and the impact of radar-derived surface precipitation rates. *Tellus* **63A** , DOI:10.1111/j.1600-0870.2010.00503.x.

Parrish, D. F. and Derber, J. C. 1992. The National Meteorological Center's spectral statistical-interpolation analysis system. *Mon. Wea. Rev.* **120**, 1747–1793.

Salby, M. 1996. *Atmospheric Physics*. Academic Press, San Diego, California. 627 pp. Cambridge University Press, Cambridge, UK. 364 pp.

Vetra-Carvalho, S., Dixon, M. A. G., Migliorini, S., Nichols, N. K. and Ballard, S. P. 2010. Breakdown of hydrostatic balance at convective scales in the forecast errors in the Met Office Unified Model. *Q. J. R. Meteorol. Soc.* submitted.

Zhang, F. 2005. Dynamics and structure of mesoscale error covariance of a winter cyclone estimated through short-range ensemble forecasts. *Mon. Wea. Rev.* **133**, 2876–2893.